Strength of fracture zones from their bathymetric and gravitational evolution

Chad E. Hall and Michael Gurnis

Seismological Laboratory, California Institute of Technology, Pasadena, California, USA

Received 9 July 2004; revised 6 October 2004; accepted 20 October 2004; published 18 January 2005.

[1] Fracture zone evolution is investigated using dynamic models that allow the fault zones to freely slip. This is an improvement over past formulations where bathymetric offsets were imposed kinematically. The models use a viscoelastoplastic rheology that incorporates the influence of fault friction on fracture zone slip history. Using viscoelastic plates, we assess the role of small-scale convection on removal of the lowermost thermal lithosphere beneath fracture zones. Through a comparison of synthetic gravity to free-air gravity across fracture zones we find that the amplitude of the gravity jump across fracture zones is best fit by models with weak faults that have depth-averaged yield strengths <10 MPa. Fracture zones with such low strengths can convert to subduction zones with ~100 km of convergence. Many fracture zones do not fit plate subsidence models with locked or slipping faults but are better fit by systems that are tectonically deformed by modest amounts of extension.

Citation: Hall, C. E., and M. Gurnis (2005), Strength of fracture zones from their bathymetric and gravitational evolution, *J. Geophys. Res.*, *110*, B01402, doi:10.1029/2004JB003312.

1. Introduction

[2] Fracture zones, common features of the oceanic lithosphere that bound seafloor of discontinuous age, are the intraplate extension of transform faults where active strike-slip motion occurs. After transform faults evolve into fracture zones, the contact separating discontinuous lithosphere may "heal" or strengthen [*Wessel and Haxby*, 1990], so that fracture zones may not be weaker than normal oceanic lithosphere [*Haxby and Parmentier*, 1988]. In contrast, tectonic uplift [*Bonatti*, 1978] and volcanic activity [*Lowrie et al.*, 1986] localized at fracture zones suggest that they are zones of weakness that may facilitate changes in plate motions during stress reorientation. Moreover, the Izu-Bonin-Mariana subduction zone [*Uyeda and Ben-Avraham*, 1972], the Puysegar-Fiordland subduction zone [*Collot et al.*, 1995], and the Hjort Trench [*Meckel et al.*, 2003] may have each initiated along an old transform fault or fracture zone. Determining the strength of fracture zones is critical for developing quantitative tests of such hypotheses.

[3] A leading argument for strong fracture zones comes from the preservation of scarp offsets formed when a transform fault first transitions to a fracture zone. At such "zero-age" fracture zones, isostatic equilibrium produces a large bathymetric step between newly formed lithosphere and the older side that has already subsided. As the lithospheric segments separated by the fracture zone cool, there are two end-member scenarios for local bathymetric evolution. If a fracture zone is sufficiently weak, slip readily occurs, the lithospheric segments act as uncoupled blocks that subside isostatically, and the bathymetric step decays. Alternatively, if a fracture zone is sufficiently strong, there is no slip at depth below the fracture, and the bathymetric step remains. However, away from the fracture zone, plate subsidence continues unimpeded, with the older, colder plate subsiding more slowly than the younger plate. Because a strong, locked fracture zone resists the differential subsidence which would act to erase the bathymetric step, the oceanic lithosphere elastically flexes [*Sandwell and Schubert*, 1982; *Sandwell*, 1984], so that the younger side is deflected upward, and the older side is locally depressed. The elastic thickness of oceanic lithosphere is temperature- and thus age-dependent, with this model predicting that the older-side troughs should be broader in comparison to the sharper, short-wavelength peaks on the younger side.

[4] All previous models of fracture zone evolution assume a kinematic boundary condition at the lithospheric age offset that implicitly fixes the topographic step at its initial value [*Sandwell and Schubert*, 1982; *Sandwell*, 1984]. In contrast, we study dynamic models in which the fracture zone at depth is free to slip, and we study a suite of cases in which the material properties of the fracture zone and oceanic lithosphere are varied. We show that oceanic lithosphere can be locally weakened at a fracture zone and can still preserve long-lived bathymetric steps that are in agreement with observed profiles of bathymetry and gravity across fracture zones. Furthermore, we expand on previous work by using models which transition from elastoplastic to viscous material behavior, allowing us to explore whether edge-driven convection may influence fracture zone evolution. Finally, we show that many of the previously unexplained

0148-0227/05/2004JB003312$09.00

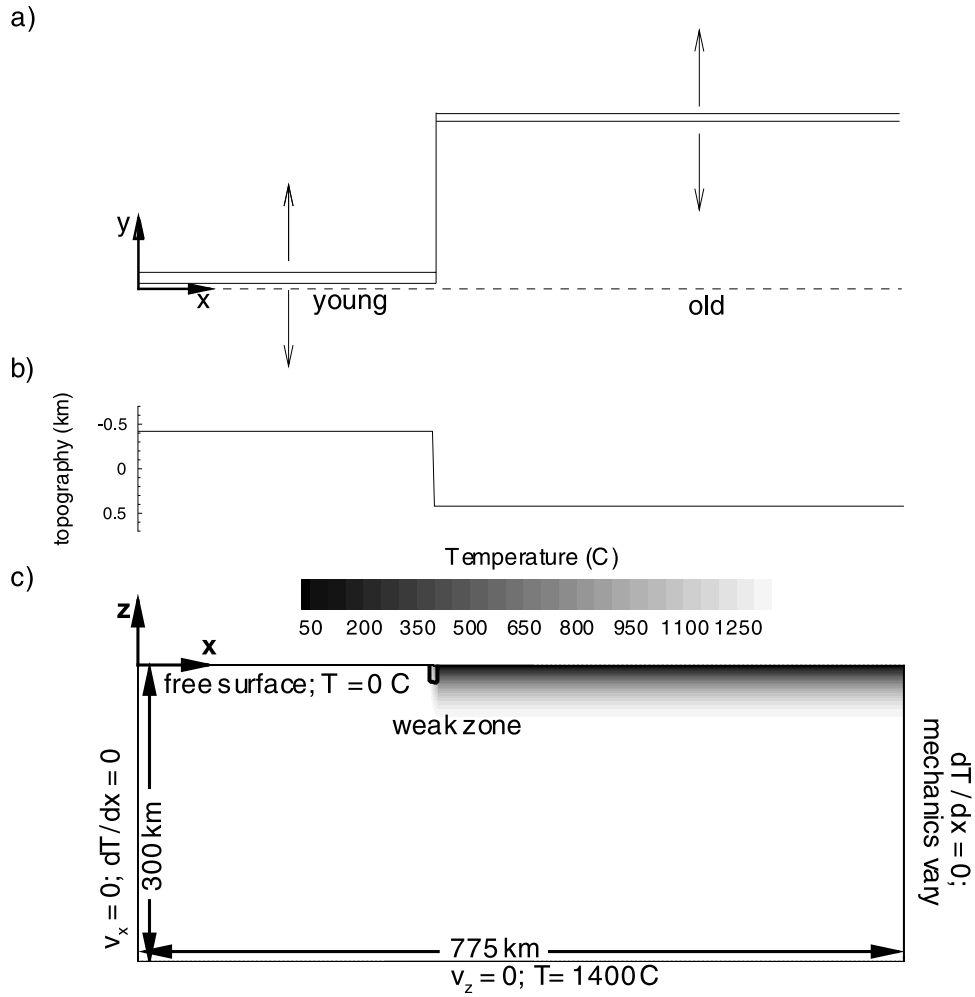

Figure 1. Schematic of initial conditions. (a) Map view schematic. (b) Initial topography. (c) Two-dimensional model domain, which is 300 km deep × 775 km wide, with the lithospheric age offset positioned 300 km from the left boundary. Resolution is variable, with 2 km × 2 km resolution in a 60 km deep × 150 km wide region centered at the age offset and 4.5 km wide × 4 km deep resolution in the lower corners.

features of fracture zones are reproduced if small amounts of extension or compression are applied.

2. Modeling Fracture Zone Evolution

[5] Our models are two-dimensional cross sections of fracture zones (Figure 1), beginning with an initial state immediately after a transform fault has transitioned to a fracture zone that is no longer offset by strike-slip motion. Initial temperature conditions are given by solutions for conductively cooled half-spaces. Three-dimensional (3-D) temperature perturbations caused by heat transport along the transform offset are not included in the initial condition, but 3-D effects do not generate substantial deviations in surface topography or create a net downward warping near a fracture zone [*Phipps Morgan and Forsyth*, 1988]. We ignore the influence of shear heating due to transform fault slip on the initial thermal field, except for one sensitivity test described in section 3. The mesh is perturbed near the free surface, so that initial topography is determined by isostatic equilibrium. The influence of an overlying water layer on isostasy is included after the calculation by scaling the model topography by $\rho_m/(\rho_m - \rho_w)$. Initially, a weakened fault zone 7 km wide by 16 km deep is placed between the two plates (Figure 1). The side and bottom boundaries have zero normal velocities and are stress-free while the top boundary is a free surface.

[6] The initial bathymetric condition used here and previously by *Sandwell and Schubert* [1982] and *Sandwell* [1984] has several implicit assumptions. First, the active transform fault is assumed to be weak such that there is no transmission of stress across it; otherwise, flexure from differential subsidence would have deflected the older plate while it bordered the active transform fault. Second, as we do not model the older plate's history before it reached the ridge transform intersection, we cannot account for flexure due to thermal bending moments during this earlier evolution [*Parmentier and Haxby*, 1986; *Haxby and Parmentier*, 1988]. Assuming that no stress transmission occurs across

Table 1. Summary of Cases Studied

Case	$\Delta\tau$, Myr	μ	C, MPa	Fault Depth, km	$\sigma_{y,ave}$, MPa	E, kJ mol^{-1}	Applied Extension, cm yr^{-1}
1	10	0	1	16	1	540	0
2	10	0	4	16	4	540	0
3	10	0	10	16	10	540	0
4	6	0	1	16	1	540	0
5	6	0	4	16	4	540	0
6	6	0	10	16	10	540	0
7	15	0	1	16	1	540	0
8	15	0	4	16	4	540	0
9	15	0	10	16	10	540	0
10	10	0	6	16	6	540	0
11	10	0	2	16	2	540	0
12	10	0.01	1	16	4	540	0
13	10	0	4	6	4	540	0
14	10	0	4	32	4	540	0
15	10	0	4	80	4	540	0
16	10	0	4	16	4	400	0
17	10	0	4	16	4	300	0
18	15	0	4	16	4	540	0.05
19	15	0	4	16	4	540	−0.05
20	15	0	1	16	1	540	0.05
21	15	0	10	16	10	540	0.05
22	15	0	30	16	30	540	0.05
23	10	0	10	16	10	400	0
24	10	0	6	16	6	300	0
25	10	0	4	16	4	540	0

active transform faults, each plate must support its own thermal bending moment, which can cause substantial flexural deflections [*Parmentier and Haxby*, 1986]. If plates are mechanically coupled along a fracture zone and the elastic thickness increases as $t^{1/2}$, where t is the thermal age of the lithosphere, the net thermal moment across the fracture zone remains constant with time, and thermal stresses would not cause further flexure [*Parmentier and Haxby*, 1986].

[7] The numerical model is based on the fast Lagrangian analysis of continua method [*Cundall*, 1989]. The explicit formulation allows the incorporation of complex nonlinear rheologies, as described by *Poliakov et al.* [1993] and *Lavier et al.* [2000]. The onset of plastic yielding is modeled using a yield potential surface which is a function of the stress tensor [*Poliakov and Herrmann*, 1994], but for ease of discussion we abbreviate "yield potential surface" to its scalar approximate "yield stress." Brittle deformation is modeled as a Mohr-Coulomb material, so that the yield stress σ_y is approximated by

$$\sigma_y = C + \mu(\sigma_n - P_f) \approx C + \mu\rho g z, \tag{1}$$

where C is the cohesion (yield strength at zero pressure), μ is the coefficient of friction, P_f is pore fluid pressure, and σ_n is normal stress, which is approximately equal to the overburden (density ρ times gravitational acceleration g times depth z). Cohesion and coefficient of friction are reduced in the model fault zone relative to regions that have not undergone plastic strain, which have C = 44 MPa and μ = 0.6 in all cases. We show in section 3 that our models can be concisely parameterized by the average yield strength $\sigma_{y,ave}$ over the depth of the fault zone z_f:

$$\sigma_{y,ave} = \frac{1}{z_f}\int_0^{z_f}[C + \mu\sigma_n(z)] \approx C + \frac{1}{2}\mu\rho g z_f. \tag{2}$$

For zero coefficient of friction the depth-averaged yield strength is equal to the fault cohesion; therefore comparison among several cases was simplified by typically setting μ to zero and varying cohesion. Table 1 lists the model parameters for all of the cases considered in this study.

[8] Previous models of the evolution of fracture zones [e.g., *Sandwell and Schubert*, 1982; *Parmentier and Haxby*, 1986] have treated the lithosphere as purely elastic with thickness set by isotherm T_{el}. For temperatures above T_{el}, viscous flow efficiently relaxes stress. In this study we use a viscoelastic (Maxwell) solid where the deviatoric strain rate tensor is given by the sum of elastic and viscous mechanisms [*Poliakov et al.*, 1993; *Gurnis et al.*, 2004], such that

$$\dot{\varepsilon}_{ij} = \frac{1}{2G}\dot{s}_{ij} + \frac{s_{ij}}{2\eta}, \tag{3}$$

where s_{ij} is the deviatoric stress tensor, G is the shear modulus, and η is viscosity. Viscous deformation is incompressible and modeled using the temperature-dependent, non-Newtonian creep of olivine [*Karato and Wu*, 1993], with viscosity

$$\eta = \eta_o\left(\frac{\dot{\varepsilon}_{II}}{\dot{\varepsilon}_o}\right)^{(1/n)-1}\exp\left[\frac{E}{nR}\left(\frac{1}{T} - \frac{1}{T_o}\right)\right], \tag{4}$$

where $\dot{\varepsilon}_{II}$ is the second invariant of the deviatoric strain rate tensor, n is the creep stress exponent, and E is activation energy.

[9] The evolution of shear zones in elastoplastic models is dependent on mesh spacing [*Lavier et al.*, 2000; *Gurnis et al.*, 2004]. Similarity of models with different mesh resolution requires that each case have the same characteristic fault offset Δx_c which is the product of shear zone width Δw and critical plastic strain ε_f, which is necessary for maximum decay of cohesion and coefficient of friction [*Lavier et al.*, 2000]. The models experience fault zone slip (<1 km) that is much less than Δx_c (3.5 km), meaning that the initially imposed fault geometry does not grow or change orientation as in studies with large applied extension or convergence [e.g., *Lavier et al.*, 2000; *Hall et al.*, 2003; *Gurnis et al.*, 2004].

3. Model Behavior

[10] Before comparing model results with transects across Pacific fracture zones, we first describe how fracture zone models with weak fault zones vary in comparison to previous models with no slip. The amount of slip across modeled fracture zones depends on integrated yield strength (Figures 2 and 3a). If a fracture zone has large yield

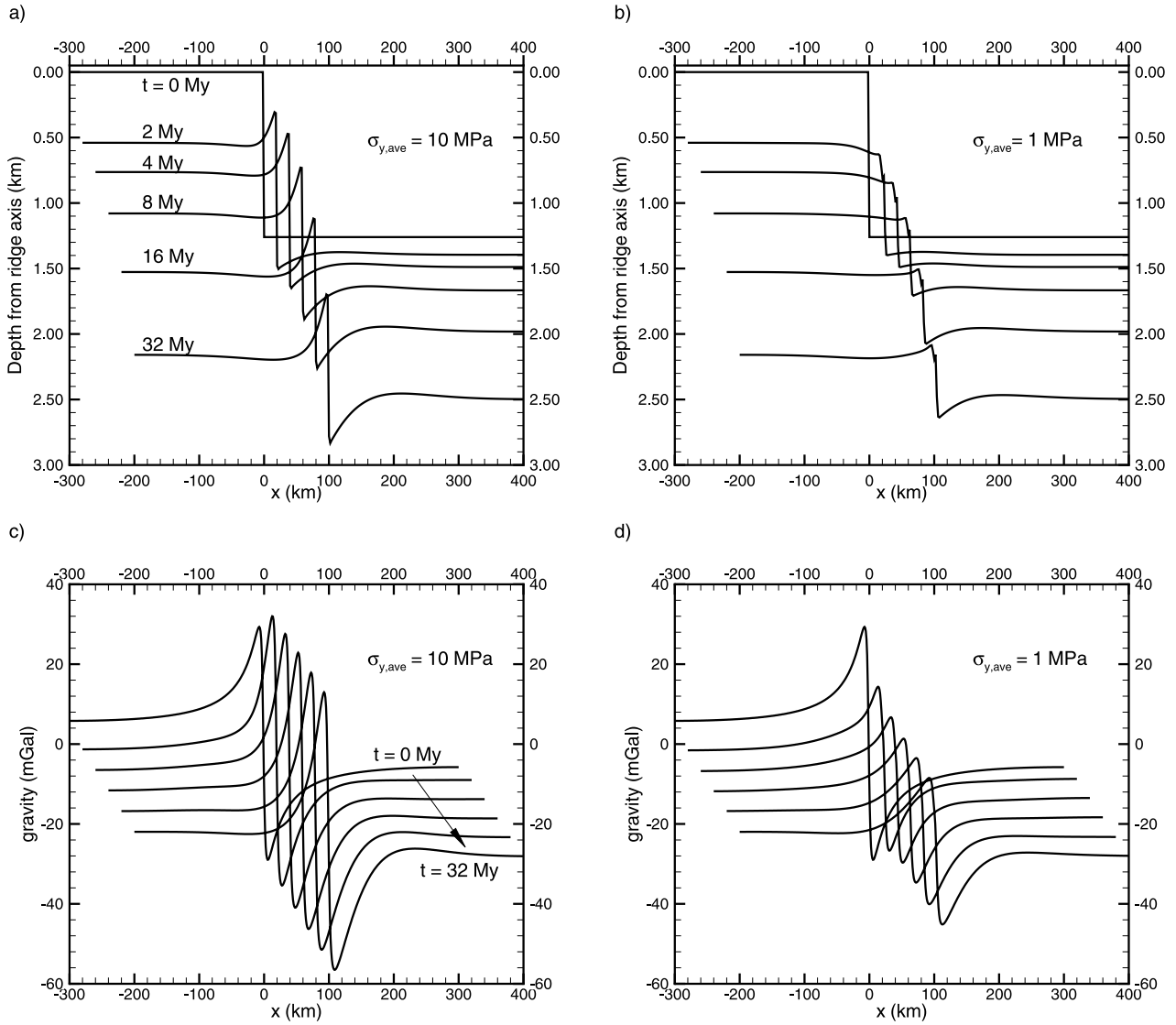

Figure 2. Evolution of (a and b) bathymetric and (c and d) gravity profiles across a model fracture zone with a 10 Myr age offset. The model fault zones have an average integrated yield strength of 10 MPa (case 3) (Figures 2a and 2c) and 1 MPa (case 1) (Figures 2b and 2d). All profiles are consecutively offset horizontally by 20 km to aid visualization. The vertical shift in bathymetric profiles occurs because of seafloor subsidence, while gravity profiles are offset consecutively by 5 mGal. Labels refer to the age of the younger-side lithosphere.

strength, slip will not occur, and differential subsidence can be accommodated purely by elastic flexure. If flexural stress in the fault zone equals the yield stress, differential subsidence will be partially accommodated by slip. Slip reduces the flexural increment and lowers the stress that would occur for a locked fault, maintaining fault stress at the yield level.

[11] Bathymetry and gravity evolve differently for locked versus slipping fracture zones (Figure 2). For a fracture zone with a 10 Myr age offset and a fault zone with $\sigma_{y,\mathrm{ave}} = C = 10$ MPa most of the load due to differential subsidence is accommodated elastically, although in the first 5 Myr a small amount of slip occurs (Figure 3a). Flexural topography due to differential subsidence leads to the pronounced younger-side highs and older-side lows typical of most "locked-fault" models [*Sandwell and Schubert*, 1982; *Sandwell*, 1984]. For the same age offset and average yield strength reduced to 1 MPa, model evolution is quite different (Figure 2b). For the first ~5 Myr the bathymetric offset across the fracture zone approaches the limit of uncoupled blocks slipping to isostatic levels (Figure 3a). A younger-side high created by elastic flexure does not begin to form until after stresses due to differential subsidence decay below the yield stress.

[12] The amplitude of the bathymetric offset and peak-to-trough gravity (Δg) at mature fracture zones is largely determined by the first 10 Myr of subsidence (Figure 3b). Differential subsidence rates across fracture zones are greatest when fracture zones are young and decay as fracture zones age [*Sandwell and Schubert*, 1982]. The stresses induced by differential subsidence σ_{sub} decay proportionally

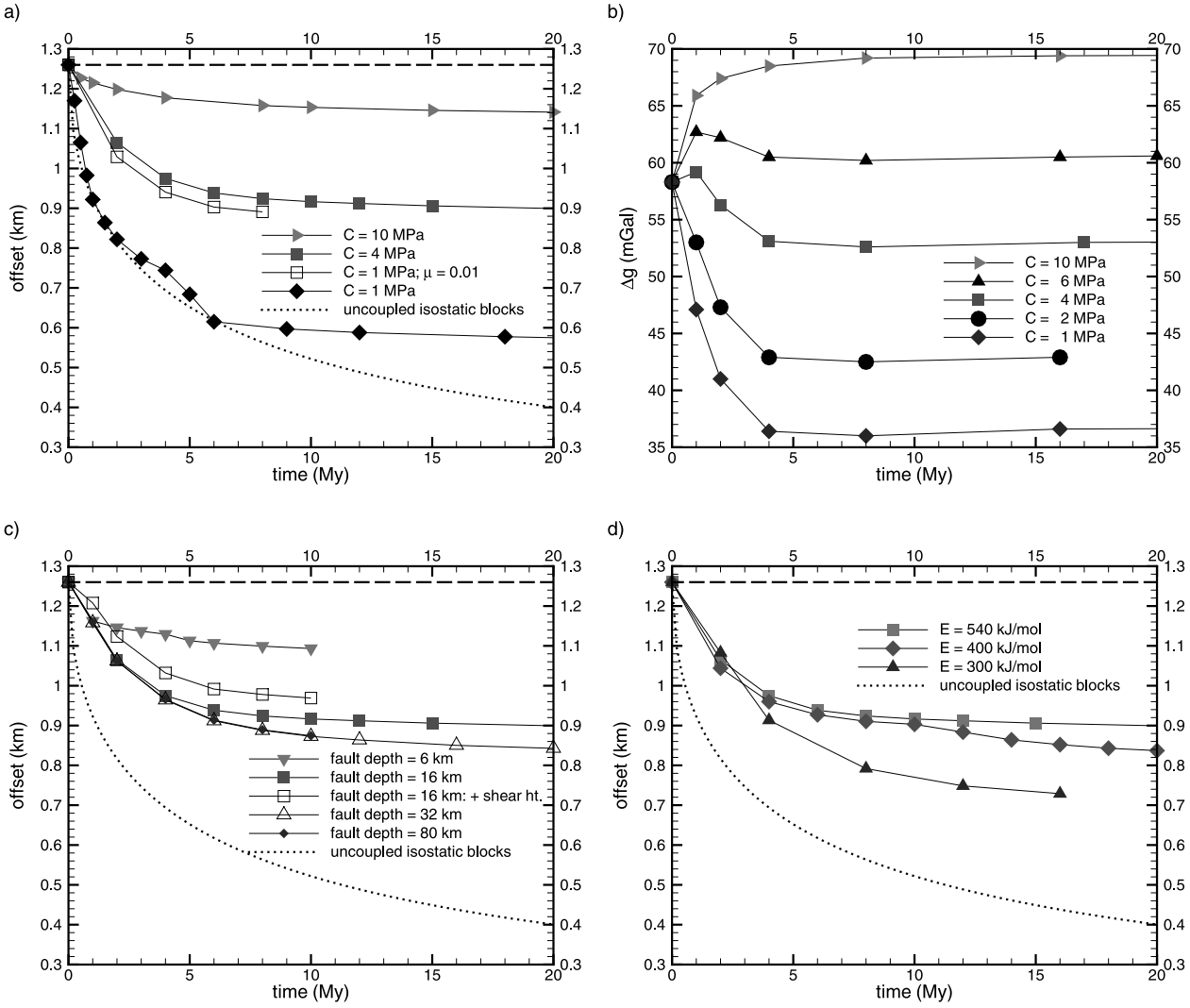

Figure 3. Evolution of maximum bathymetric offset (depth of younger-side high minus older-side low) across model fracture zones with 10 Myr age offset as a function of (a) cohesion, (c) fault depth, and (d) activation energy. (b) Evolution of peak-to-trough gravity amplitudes (Δg) versus integrated yield strength. Case 2 is plotted in each frame as a reference model. Except where noted otherwise, faults in the experiments have zero coefficient of friction ($\sigma_{y,\mathrm{ave}} = C$), cohesion of 4 MPa, depths of 16 km, and activation energy of 540 kJ mol^{-1}. In Figure 3a the models with open and solid squares have approximately identical $\sigma_{y,\mathrm{ave}}$, verifying that integrated strength is a sufficient parameter for characterizing slip in fracture zones. In Figure 3c we show one case (case 25) which considers shear heat in the initial thermal condition.

to the decay in flexural increments of locked-fault models. Taking the time derivative of *Sandwell and Schubert* [1982, equation (4)] gives

$$\frac{d\sigma_{\mathrm{sub}}}{dt} \approx -\rho_m g \alpha T_m \left(\frac{\kappa}{\pi}\right)^{1/2} \left\{ t^{-1/2} - (t + \Delta\tau)^{-1/2} \right\}, \quad (5)$$

where ρ_m and T_m are the reference mantle density and temperature at depth, respectively, α is the coefficient of thermal expansion, κ is thermal diffusivity, and $\Delta\tau$ is the age offset across the fracture zone. During the initial stage of model evolution, σ_{sub} may exceed σ_y, in which case slip occurs. As the rate of differential subsidence decays, σ_{sub} drops below the yield stress, slip ceases, and the offset is nearly constant at later times (Figure 3).

[13] Free-air gravity for the models is calculated by summing the contributions due to the density contrast from seafloor topography and from thermal density variations in the mantle (Figures 2c and 2d). The models do not account for any gravity signature due to Moho topography. All model gravity profiles exhibit younger-side peaks and older-side troughs. The gravitational contributions from topography and thermal density variations at depth do not completely cancel at fracture zones, giving rise to gravity profiles which have the same form as that of a flexed topographic load seen subsequently, as seen in the isostatic gravity profile at $t = 0$. Therefore adjacent high-low lineations in seafloor gravity

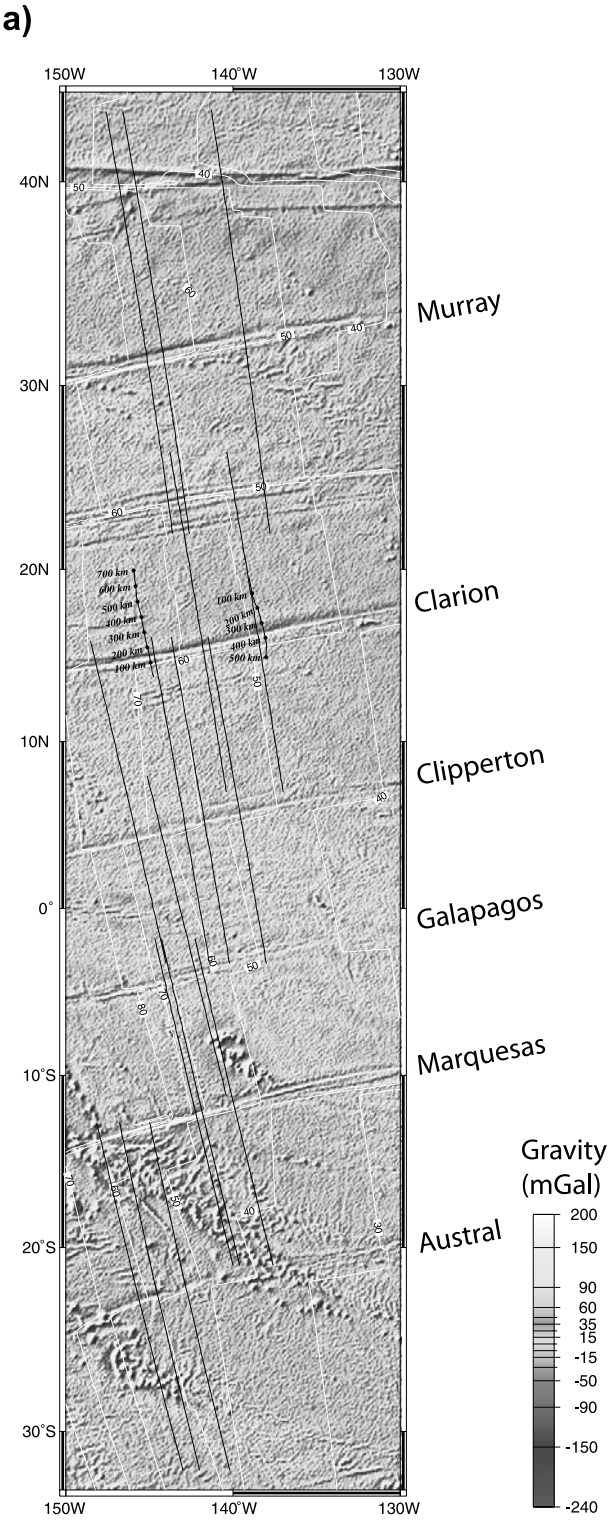

Figure 4. (a) Selected gravity profiles (black lines) across Pacific fracture zones. Black lines with circles at 100 km intervals are shipboard bathymetry profiles from survey HU931009. (b) Gravity profiles across the Udintsev and Menard fracture zones. The eastern and western branches of these fracture zones lie within the Antarctic and Pacific plates, respectively. Free-air gravity (shaded) is from *Sandwell and Smith* [1997] while seafloor age isochrons (white contours) are from *Müller et al.* [1997]. See color version of this figure at back of this issue.

are not necessarily due to flexure at a locked fracture zone but could be due to the edge effect at a discontinuity in lithospheric thickness. Many previous studies [e.g., *Parmentier and Haxby*, 1986; *Wessel and Haxby*, 1990; *Christeson and McNutt*, 1992] removed the isostatic edge effect from both data and model profiles, which slightly reduced the amplitude of peak-to-trough gravity at the fracture zone (Δg) relative to this study.

[14] The evolution of peak-to-trough gravity amplitude (Figure 3b) provides complementary information to the bathymetric evolution. For end-member cases where faults are strong enough to support large flexural loads (e.g., $\sigma_{y,\mathrm{ave}}$ = 10 MPa case), Δg increases with time as flexurally supported topography accumulates. However, for weak fault zones (e.g., $\sigma_{y,\mathrm{ave}} = C$ = 1 MPa case) the fracture zone slips at depth and Δg initially decays rapidly (more than 20 mGal in 4 Myr). For intermediate fault strength ($\sigma_{y,\mathrm{ave}} \sim$ 4 to 6 MPa), Δg is not monotonic with time. For the first ~1 Myr the vertical flexural displacement is larger than the amount of fault slip, and Δg increases. After this initial stage the amount of accumulated slip exceeds the flexural displacement, and Δg decreases. Because of the decay of differential subsidence rates with time (equation (5)), there is little sensitivity of either the bathymetric offset or Δg after ~5 Myr (Figures 3a and 3b). For all cases, after ~10 Myr, Δg increases slowly because of small amounts of continued differential subsidence, and the amplitudes of flexural bulges and moats continue to gradually grow.

[15] We performed one sensitivity test to the assumed initial thermal conditions. We explored the role of shear heating due to transform fault slip by introducing a perturbation T' to the thermal field of the older side of the fracture zone, reflecting shear heat that would have accumulated along the actively slipping transform. Our approximate perturbation T' was

$$T'(x') = \frac{\sigma_{y,\mathrm{ave}} V}{2k} x' \exp\left[\frac{-x'^2}{4\kappa(2\delta_{tf}/V)}\right], \qquad (6)$$

where x' is the distance from the fracture zone, V is the full rate of plate spreading, δ_{tf} is the length of the transform offset, and k is thermal conductivity. This approximate perturbation is one dimensional and is added to the older-side thermal field to a depth equal to that of the imposed fault zone. We compare a model that adds initial shear heat consistent with k = 2.5 W m^{-1} °C^{-1}, $\sigma_{y,\mathrm{ave}}$ = 4 MPa, δ_{tf} = 100 km, and V = 10 cm yr^{-1} (case 25) (Figure 3c) to a model without shear heat (case 2). Shear heating essentially reduces the thermal age of the older-side lithosphere near the fracture zone, therefore reducing the amount of differential subsidence relative to identical cases that do not consider shear heating. The bathymetric offset in our shear heating case is ~6% less than that of an otherwise identical case without shear heating, implying that the neglect of shear heating on the initial thermal field does not strongly influence our results.

4. Data Selection and Analysis

[16] We compared transects of observed gravity [*Sandwell and Smith*, 1997] across several Pacific fracture

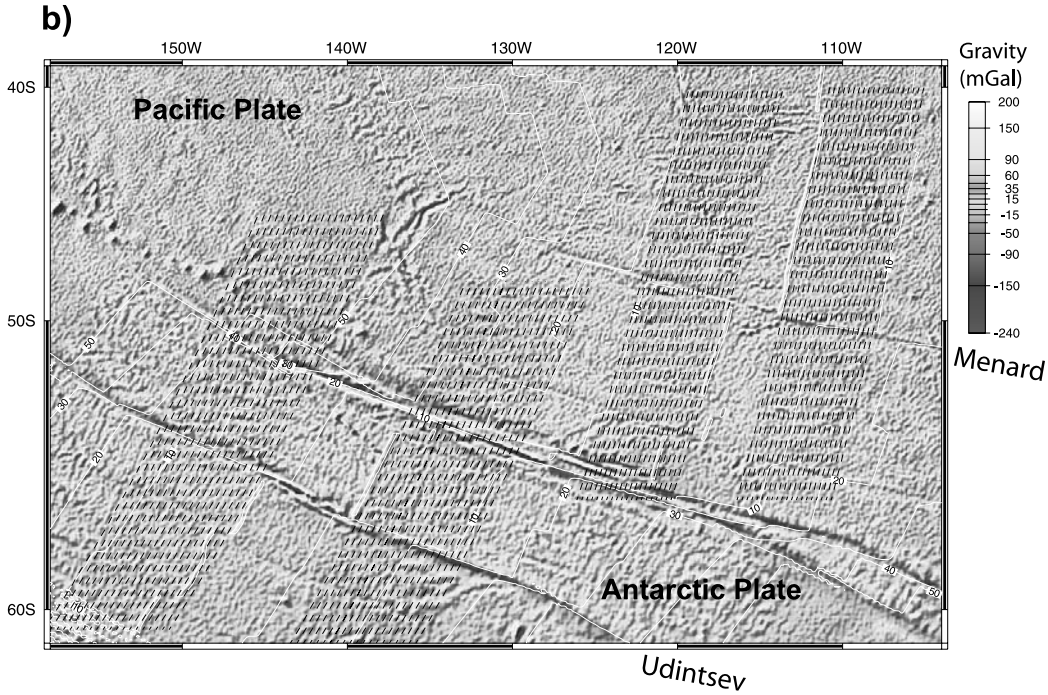

Figure 4. (continued)

zones (Figures 4a–4b) to predictions. For this study we neglect fracture zones created at slower spreading centers, which typically have more short-wavelength roughness in bathymetry and gravity that obscures the longer-wavelength features associated with elastic plate bending. We focused on satellite-derived gravity instead of shipboard bathymetry because there are relatively few orthogonal ship profiles over long distances. We excluded transects that cross fractures zones at locations previously identified as anomalous [*McCarthy et al.*, 1996; *Kruse et al.*, 1996]. These studies inferred that many of the fracture zone crossings that depart from the predictions of locked-fault models are due to structures formed at transform faults during periods of plate reorganization that had placed the transform or young fracture zone in tension or compression. In addition, some fracture zones are either too closely spaced to act independently of one another (e.g., Mendocino-Pioneer [*Sandwell and Schubert*, 1982]) or are composed of multiple strands (e.g., Molokai) and are excluded. The seafloor age grid [*Müller et al.*, 1997] is used to determine the age offset across fracture zones. Age offsets ($\Delta\tau$) across these fracture zones range from 6 to 16 Myr.

[17] Gravity and bathymetry profiles across the Clarion fracture zone (Figure 5) display large peak-and-trough patterns, which we required for inclusion in our data. Comparison to models shows that the ~80 km nearest the fracture zone on the older side has higher than expected gravity and slightly higher than predicted bathymetry. This region of elevated gravity on the older side is present in most of the mature fracture zones of the Pacific (Figure 6). This uplifted region on the older side has previously been attributed to flexure from thermal bending stresses that accrued along active transform faults [*Parmentier and Haxby*, 1986; *Haxby and Parmentier*, 1988; *Wessel and Haxby*, 1990]. Peak-to-trough gravity across the easternmost crossing of the Clarion is best fit with $\sigma_{y,\mathrm{ave}}$ between 4 and 10 MPa (Figures 5a and 5b). Both of these models slightly underpredicted the amplitude of the step in bathymetry. However, we note that the observed bathymetric step in Figure 5c (>1800 m) exceeds that predicted for a locked isostatic model (~1200 m), indicating that the younger-side high in this profile is probably amplified by tectonic or volcanic activity.

[18] In the Pacific we were left with six fracture zones (Figures 4a–4b), from which we extracted gravity along perpendicular profiles and measured the peak-to-trough gravity amplitude (Δg) at the fracture zone. As expected, Δg is positively correlated with age offset (Figure 7), consistent with observed increases in geoid amplitudes with $\Delta\tau$ [*Wessel and Haxby*, 1990]. By overlaying the predicted Δg from numerical experiments where we varied the average yield strength from 1 to 10 MPa, we see that the data cluster around the trend for $\sigma_{y,\mathrm{ave}}$ = 4 MPa. We emphasize, however, that the data selection process was biased toward selecting profiles that had large Δg and more closely mimicked locked-fault models; the data compiled in Figure 7 are thus biased toward higher predicted fault strength. We further note that the model trends in Figure 7 would be displaced toward higher Δg if shear heat had been considered in the initial thermal condition, which would push the estimated fault strength lower, though only slightly.

[19] Modeled faults which best fit gravity amplitudes across fracture zones, with an integrated yield strength of only 4 MPa, are extremely weak compared with laboratory estimates of the frictional strength of rocks. For a standard laboratory value of μ = 0.6 [*Byerlee*, 1978] and zero cohesion a mantle shear zone extending to depths of 16 km would have an average yield strength exceeding 150 MPa (equation (2)). For the same shear zone to have

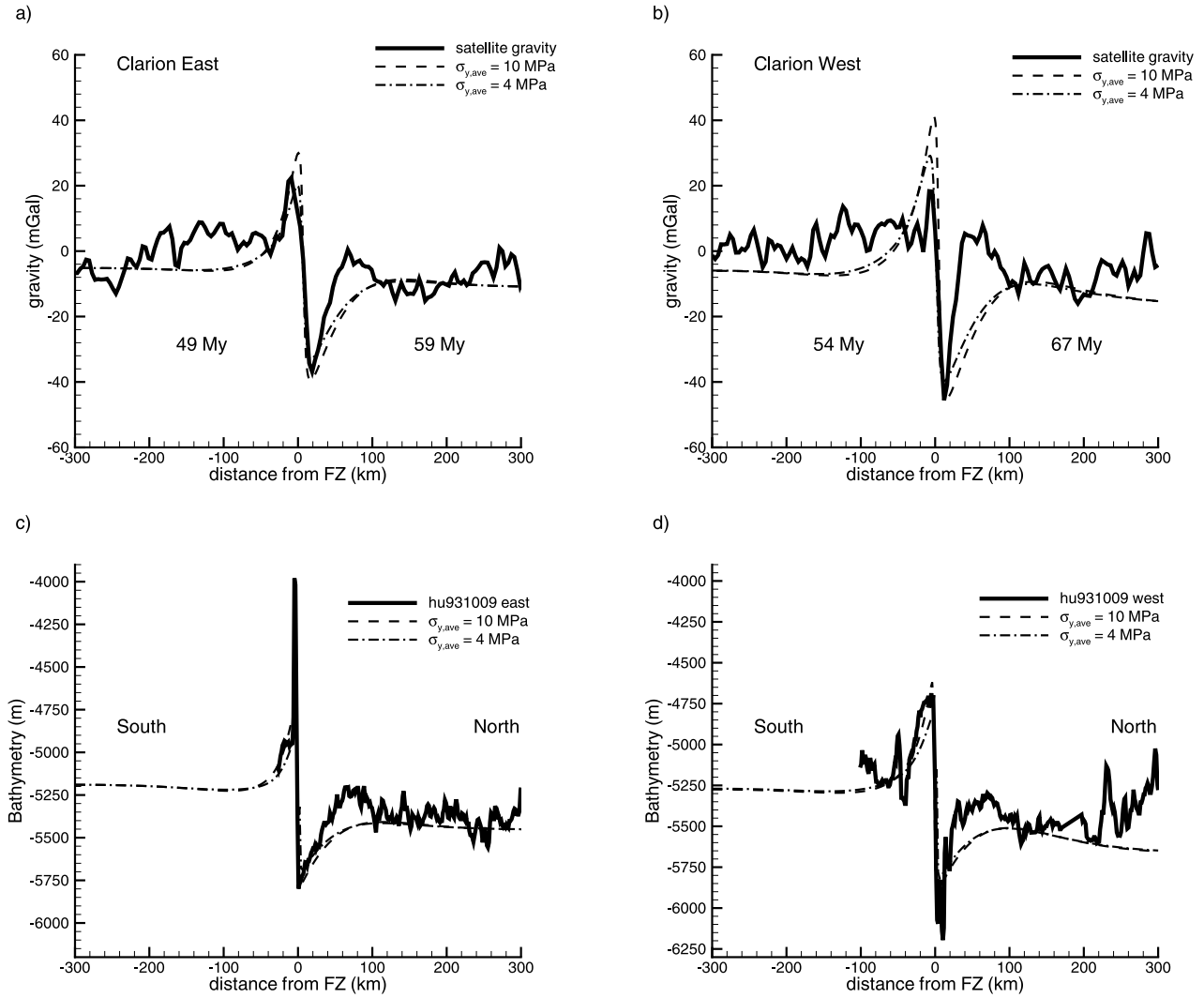

Figure 5. (a and b) Free-air gravity extracted along profiles perpendicular to the Clarion fracture zone (solid lines), with fracture zone age and age offset labeled (see legend). Dashed and dot-dashed lines show model predictions from differential subsidence models where the average yield strength is varied. The younger side of the fracture zone is to the left in each profile. (c and d) Bathymetry from survey HU931009 (solid lines) and predicted bathymetry. For the location of gravity and bathymetry profiles, see Figures 4a–4b. Figures 5a–5d are not labeled on Figures 4a–4b.

$\sigma_{y,ave}$ of only 4 MPa would require an effective coefficient of friction of ~0.02.

5. Influence of Small-Scale Convection

[20] Earlier studies of fracture zone evolution treated the lithosphere as purely elastic and ignored viscous deformation. Depending on the sensitivity of viscosity to temperature, the lowermost thermal lithosphere may deform viscously (Figure 8). For models with an activation energy consistent with dislocation creep of dry olivine (540 kJ mol^{-1}) [e.g., *Karato and Wu*, 1993] the thermal lithosphere behaves almost purely elastically, and viscous flow of the lowermost lithosphere is not important.

[21] Reducing activation energy is analogous to lowering T_{el} and reducing elastic thickness, so that viscous deformation of the lower lithosphere is enhanced. For a lower bound model with E = 300 kJ mol^{-1}, consistent with diffusion creep of dry olivine [*Karato and Wu*, 1993], viscous flow removes the lowermost ~15 km of the thermal lithosphere beneath a fracture zone (Figure 8b). While our models are in isostatic equilibrium, lateral pressure differences across the fracture zone are present above the compensation depth. These horizontal pressure gradients drive viscous flow, with a vigor increasing as activation energy decreases. Viscous removal of the lowermost lithosphere results in shoaling of bathymetry on the older side of a fracture zone. Gravity profiles from models exhibiting small-scale convection (Figure 8c) have a small high in apparently the correct location, but not of sufficient amplitude, to match observed profiles. This mode of convective thermal boundary layer removal is restricted to within ~80 km of the fracture zone and thus cannot explain the older-side (younger-side) geoid lows

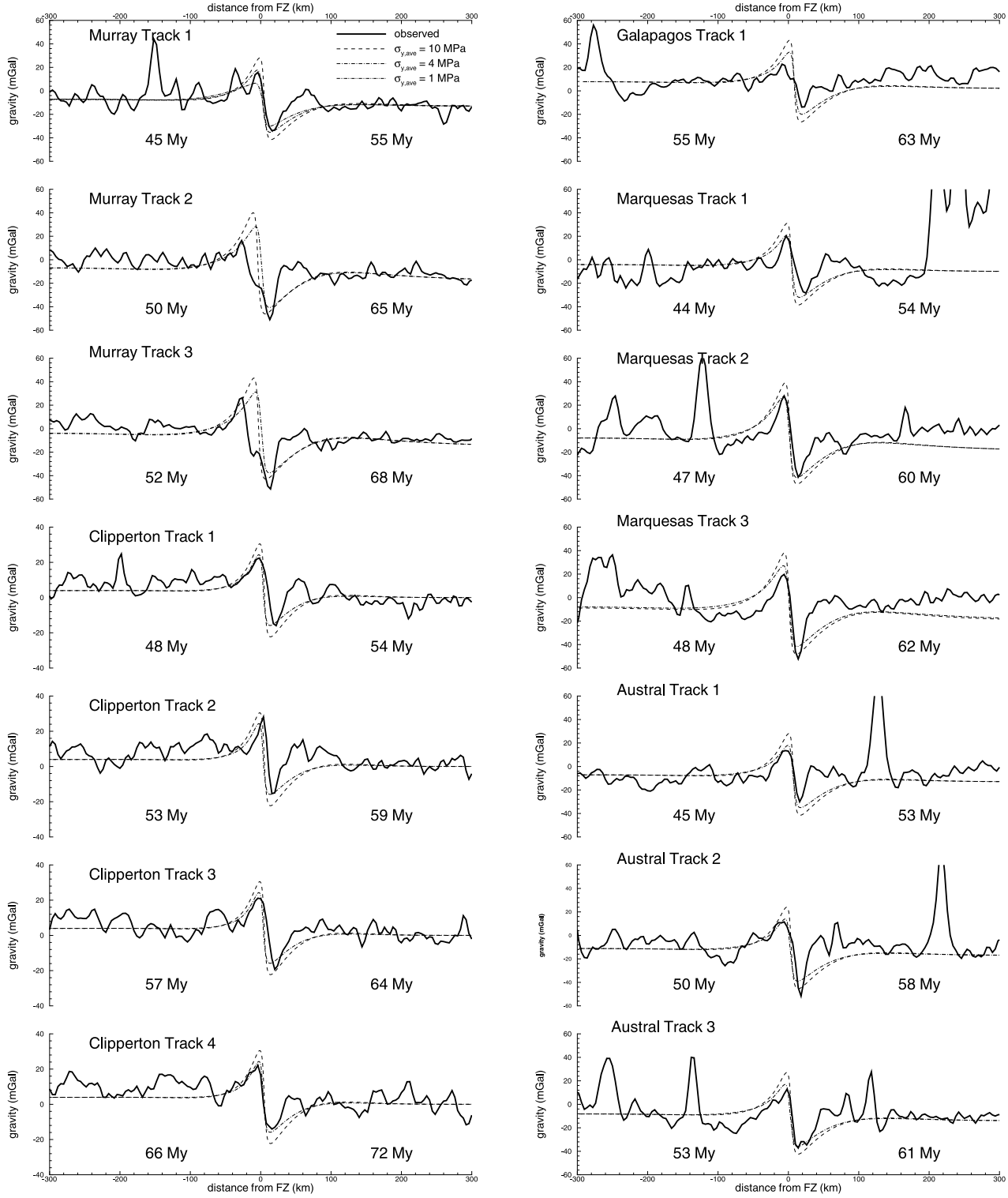

Figure 6. Satellite free-air gravity profiles from Figures 4a–4b versus predictions from models with slipping faults. Profiles for each fracture zone are numbered from youngest crossing to oldest (i.e., right to left on the map). Best fitting models were selected from cases 1–9.

(highs) centered 100–150 km from the fracture zone [*Wessel and Haxby*, 1990]. The models also indicate interaction between viscous delamination and slip at the fracture zone, which causes Δg to be too low in cases undergoing delamination (Figure 8c). For a case with E = 400 kJ mol^{-1}, viscous delamination begins at ~10 Myr. Surface topography most rapidly changes when a mature drip separates from the thermal boundary layer, which induces stresses sufficient to cause slip in the fault zone. Slip induced by topographic adjustment occurs at ~4 and ~12 Myr for an

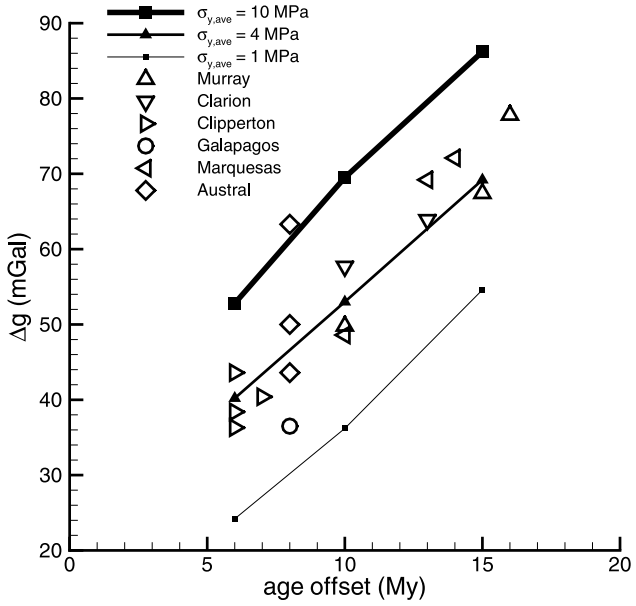

Figure 7. Peak-to-trough gravity (Δg) at fracture zones as a function of age offset. Predicted Δg are obtained by running numerical experiments to at least 20 Myr (cases 1–9), after which there is little change in amplitude.

activation energy of 300 and 400 kJ mol^{-1} (Figure 3d), respectively. We varied both the average yield strength and activation energy but were unable to find a suitable set of parameters which simultaneously matched both the amplitude of the older-side highs and the peak-to-trough amplitude at fracture zones.

6. Tectonic Evolution of Fracture Zones

[22] Gravity profiles across old segments of fracture zones (>10 Myr) reflect both the material properties of fracture zones as well as their integrated history. Since the magnitude of bathymetric scarps and peak-to-trough gravity at fracture zones should change most quickly during the first 10 Myr of evolution, we attempted to further constrain the strength of fracture zones, as well as their duration of weakness, at southern Pacific fracture zones that extend back to a spreading center.

[23] The Udintsev fracture zone (at 53°–59°S, offsetting the Pacific-Antarctic Ridge) has a large age offset (12–15 Myr), but its mechanical state may be complicated by the influence of other nearby fracture zones that compose the Eltanin Transform Fault system [*Lonsdale*, 1994] (Figure 4b). The Menard fracture zone (along 48°–51°S) has a smaller age offset (6–8 Myr) but is farther away from neighboring fracture zones (Figure 4b). For each of these fracture zones we extracted gravity [*Sandwell and Smith*, 1997] and seafloor age [*Müller et al.*, 1997] along fracture zone–perpendicular profiles at small age intervals (0.5–1.0 Myr) for their first 15 Myr of evolution. Along the Menard fracture zone, Δg over this age interval typically lies between 20 and 50 mGal (Figure 9a), within the bounds of models with $\sigma_{y,ave}$ of 1–4 MPa but consistently below that predicted for $\sigma_{y,ave}$ of 10 MPa. On the eastern (Antarctic) branch, there is a more pronounced decay of Δg with age compared to the western (Pacific) branch, which has no

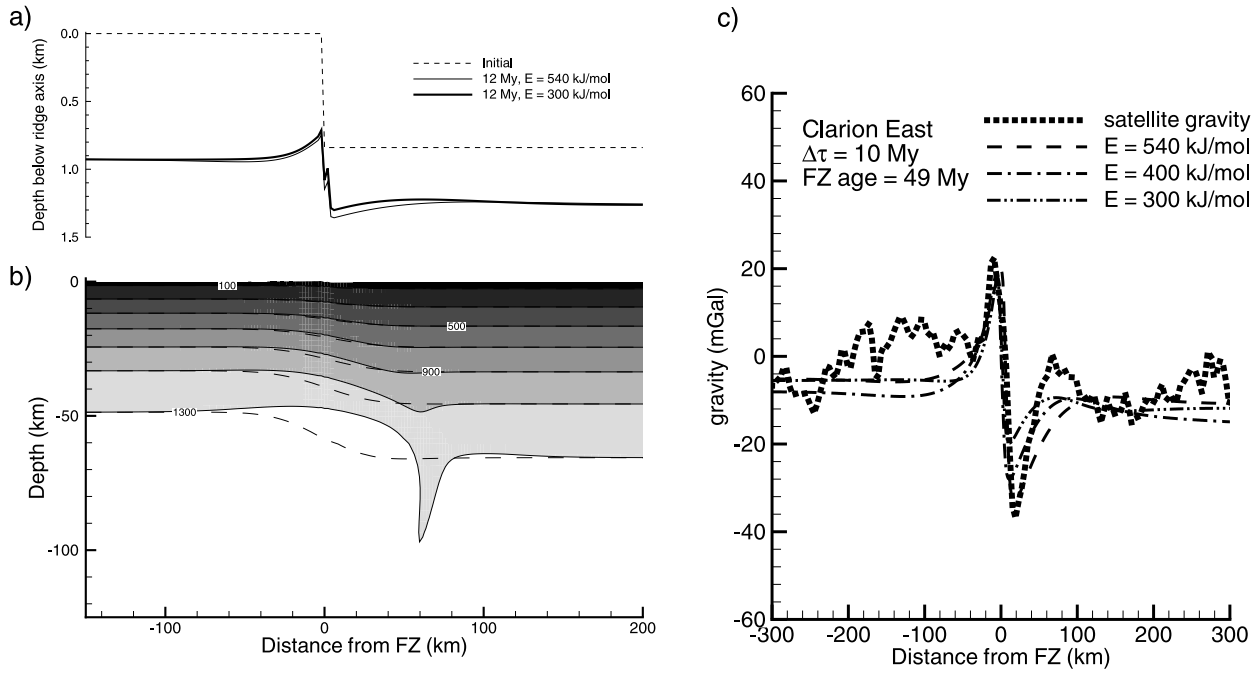

Figure 8. Influence of activation energy on (a) topography, (b) temperature field, and (c) gravity at fracture zones. All models in this example have $\sigma_{y,ave}$ = 4 MPa and an age offset $\Delta\tau$ of 10 Myr (cases 2 and 16–17). In Figure 8b, shaded contours are for a model with E = 300 kJ mol^{-1} while dashed contours are for E = 540 kJ mol^{-1}, both for instances where the age of the younger lithosphere is 12 Myr. Gravity profiles in Figure 8c are for models where the age of the younger lithosphere is 50 Myr. Location of the profile extracted from the satellite gravity grid is given in Figure 4a.

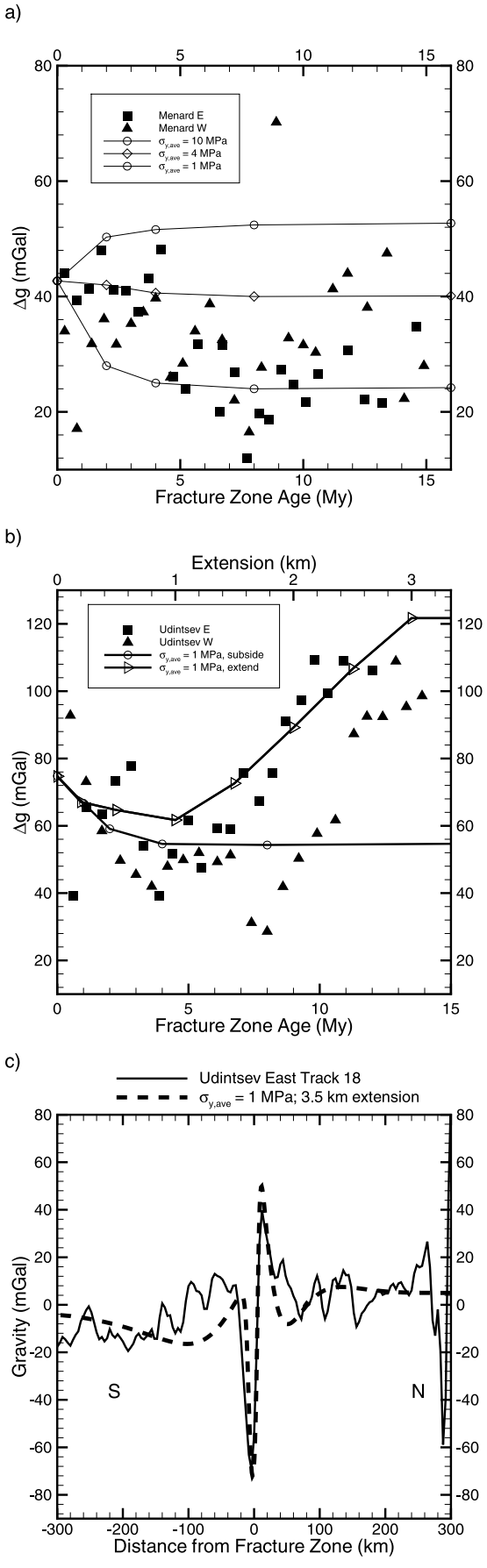

Figure 9. (a) Peak-to-trough gravity as a function of age of the Menard fracture zone. Squares are for transects crossing the eastern (Antarctic) branch, and triangles are for transects crossing the western (Pacific) branch. Curves linking open symbols reflect models of fracture zone subsidence with average yield strengths of 4 MPa (diamonds) and 1 MPa (circles). (b) Peak-to-trough gravity as a function of age of the Udintsev fracture zone, with symbols as in Figure 9a. The curve linking open circles is for a model which subsides with no applied extension, while the curve linking open triangles is for a model undergoing extension at a fixed rate of 0.02 cm yr^{-1}. (c) Comparison of model with $\sigma_{y,ave}$ = 1 MPa and $\Delta\tau$ = 15 Myr (case 20) that has undergone 3.5 km of extension versus observed profile crossing the Udintsev fracture zone at 130°W.

significant trend. For the Udintsev fracture zone the evolution of Δg with age disagrees with predictions from any model where lithospheric segments passively subside (Figure 9b). For both its eastern and western branches, Δg decays for ages less than ~5 Myr but increases rapidly for ages greater than this. Progressing from the youngest section to that which formed at 10 Ma, the age offset across the Udintsev fracture zone increases from ~13 to >15 Myr. This moderate increase in $\Delta\tau$ should only perturb Δg by ~8 mGal, while the observed increase for sections older than 5 Myr exceeds 50 mGal.

[24] Fracture zones can be placed under tension or compression during changes in plate motions [*Menard and Atwater*, 1968, 1969]. We modeled the evolution of fracture zones under moderate amounts of extension or convergence by either pulling outward or pushing inward, respectively, at a prescribed velocity on the upper right boundary of the model while keeping the left side fixed. On the lower half of the right boundary the sign of the imposed velocity is reversed so that volume is conserved [see *Hall et al.*, 2003].

[25] Fracture zones placed either in extension or compression will develop distinctive morphological features after only ~2 km of differential motion (Figure 10). Fracture zones that undergo extension develop a deep central valley flanked by transverse ridges (Figures 10a and 10b). An older-side ridge is first seen in model bathymetry after ~2 km of extension and begins to be clearly seen in model gravity profiles after ~3 km of extension. Older-side highs near the fracture zone cannot be explained by differential subsidence models with or without slip but can be fit by our models of fracture zones that have undergone modest amounts (a few kilometers) of extension. We found that extensional models of fracture zones with average yield strengths ranging from 1 to 10 MPa are qualitatively similar. All extensional models with $\sigma_{y,ave} \leq 10$ MPa develop Δg of 100 mGal within ~2.4–2.6 km of extension, whereas Δg for a model with a stronger average yield strength of 30 MPa does not reach 100 mGal until almost 5 km of extension. The morphology of the transverse ridges does not vary substantially as a function of fault strength, but models with stronger faults tended to have deeper troughs flanking the younger-side high. Even in the case of the strongest fault placed in extension (case 22), extension remains localized

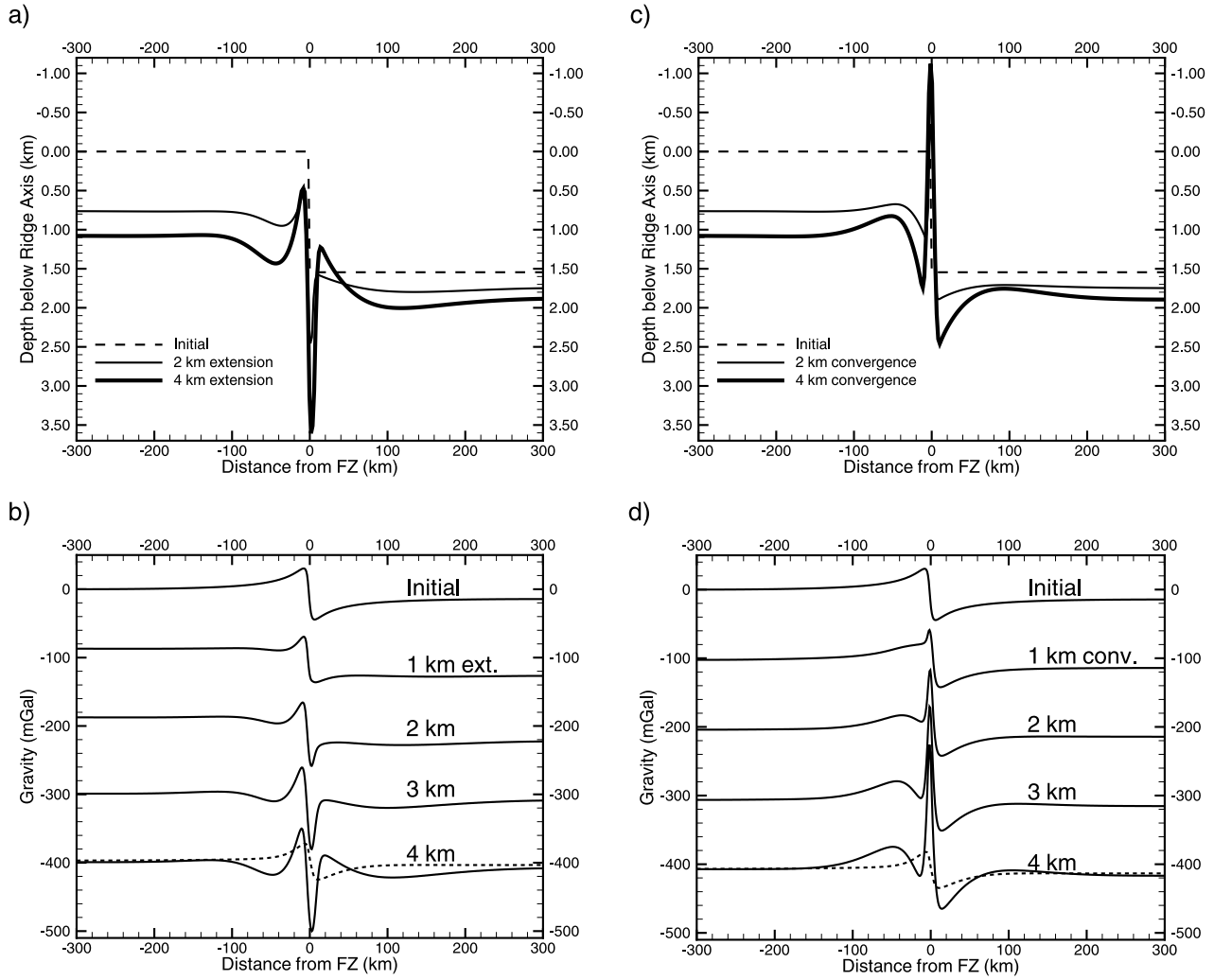

Figure 10. Models of (a and b) forced extension and (c and d) convergence of a fracture zone. Models have an age offset $\Delta\tau$ of 15 Myr and $\sigma_{y,ave}$ = 4 MPa (cases 18 and 19). Models were run for 8 Myr (4 km of net extension or convergence), beginning with zero-age younger-side lithosphere, and have rates of extension or convergence of 0.05 cm yr^{-1}. Bathymetry profiles (Figures 10a and 10c) are offset by isostatic subsidence, while gravity profiles (Figures 10b and 10d) are arbitrarily offset by 100 mGal for clarity. Gravity profiles at t = 8 Myr (4 km extension/convergence) are compared against models with no external horizontal force (short-dashed line).

within the weakened area centered on the fracture zone, and secondary normal faults do not form within the range of net extension (<10 km) explored here.

[26] The Udintsev transform and fracture zone were placed in tension by a change in Pacific-Antarctic relative plate motion in the Pliocene [*Lonsdale*, 1994]. From the seafloor age grid [*Müller et al.*, 1997] the current offset across the Udintsev fracture zone is ~2 Myr less than that at 10 Ma. During periods of extension, transform offsets get shorter [*Tucholke and Schouten*, 1988], and the age offset across them decreases, provided that spreading rates remain constant. The decrease in $\Delta\tau$ across the Udintsev fracture zone since ~10 Ma is thus consistent with the transform and young fracture zone being placed in tension. For the Udintsev and surrounding transform faults (i.e., the Eltanin system), there are 99 earthquakes with cataloged focal mechanisms. Of these, most have the expected strike-slip geometry, but eight earthquakes have normal faulting mechanisms with consistently oriented tensional axes which indicate that ongoing secondary extension is superimposed on the predominantly strike-slip motions across the Eltanin system [*Okal and Langenhorst*, 2000].

[27] The observed change in Δg with age of the Udintsev fracture zone can be reproduced by extending a fracture zone with $\Delta\tau$ = 15 Myr at a rate of 0.02 cm yr^{-1} (Figure 9b). Gravity for a model of 3.5 km of fracture zone extension matches, in amplitude, both the observed peak-to-trough drop and older-side high (Figure 9c). However, the observed ridges on both the younger and older sides are wider than those predicted. Although a full exploration is outside the scope of this paper, we note that the bathymetric ridges that form in our extensional models resemble transverse ridges that are observed along the transform faults of slow spreading centers (e.g., the Romanche or Vema

transforms) [e.g., *Bonatti*, 1978; *Bercovici et al.*, 1992], suggesting that the transverse ridges may arise because of moderate extension across these transforms.

[28] Models of converging fracture zones have several identifiable features that distinguish them from extended or nontectonic fracture zones. On the younger side, fracture zones in convergence develop a broad (~80 km) rise within 100 km of the lithospheric contact, whereas simple subsidence models are flat (Figure 2) and extensional models have a broad trough. Moving toward the fracture zone, the younger-side rise descends steeply into a trough whose termination marks the onset of a narrow (~20 km) ridge. This ridge is created by extrusion of the weak fault zone material upward, deforming the free surface at the top of the model. If there is sufficient convergence (>2 km) in the models, uplift of this tectonic sliver outpaces isostatic subsidence, and the ridge ascends to depths shallower than the spreading center axis. On the older side a trough develops which is much broader and deeper than that of a differential subsidence model (dashed line in Figures 10c and 10d).

7. Discussion

[29] Assuming that forces from differential subsidence, not tectonics, dominate the evolution of Pacific fracture zones, gravity offsets are consistent with weak faults which support 10 MPa or less (Figure 7). Our study is consistent with earlier conclusions on the strength of the Marquesas fracture zone, where only 2 out of 32 satellite altimetry (and 0 out of 27 shipboard bathymetry) profiles were consistent with locked-fault (i.e., strong fault) models [*Christeson and McNutt*, 1992]. Using observed free-air gravity anomalies as proxies of vertical forces, shear stresses along the Marquesas [*Christeson and McNutt*, 1992] and Molokai [*Bonneville and McNutt*, 1992] fracture zones are typically 10 MPa or lower, <25% of the magnitude necessary to support the loads of locked-fault models. For the Marquesas fracture zone, gravity profiles associated with weak segments extend beyond its intersection with hot spot tracks, so the hot spots cannot be invoked as an origin for the widespread weakness. Other mature Pacific fracture zones (Mendocino, Murray, and Clipperton) are reasonably fit by locked-fault models, while the Clarion fracture zone is seemingly divided between a western section fitting the locked-fault model and a section farther east that appears weak [*Bonneville and McNutt*, 1992].

[30] Weak fracture zones would represent significant lithospheric heterogeneities and would likely play an important role in accommodating changes in plate motion or in the formation of new plate boundaries. *Hall et al.* [2003] showed that if fracture zones are not locally weakened, convergence across them is accommodated by distributed buckling of the younger-side lithosphere. If, however, fracture zones have low yield strengths (<20 MPa), prolonged convergence remains localized within the weak fault zone and can lead to self-sustaining (i.e., buoyancy-dominated) subduction after ~100–200 km of convergence. Our present study shows that Pacific fracture zones are weak, having integrated yield strengths below 10 MPa for at least their first ~5 Myr. Additional modeling has shown that if a fracture zone can support stresses of only 10 MPa or less, net plate convergence of 100–160 km across it will lead to the formation of a new, self-sustaining subduction zone [*Hall et al.*, 2003].

[31] Abyssal peridotites dredged from fracture zones are typically serpentinized [e.g., *Dick*, 1989]. Further evidence that fracture zones may be extensively serpentinized comes from both active seismic surveys of fracture zones [*Muller et al.*, 1997] and field studies of ophiolites [*Saleeby*, 1979]. Serpentinized mantle is significantly weaker than most rocks ($\mu = 0.4$ [*Escartin et al.*, 1997]) and should promote slip in fracture zones. However, a serpentinized fault zone (drained of the fluid which caused serpentinization) will have an average yield strength exceeding 10 MPa if it is deeper than ~2 km. One possibility for creating an effectively low coefficient of friction is that the seawater which infiltrates the fracture zone and causes serpentinization attains pore pressures that approach lithostatic levels, which reduces the effective coefficient of friction to zero (equation (1)). High pore fluid pressure would not need to be constantly maintained; P_f would only need to reach near-lithostatic levels intermittently so that the fracture is weak over timescales of 10^5 years. An alternative explanation for the weakness of fracture zones is that the normal stress is not simply the lithostatic overburden but is instead much lower, perhaps because of thermal stresses. In this hypothesis, transform faults are tensile cracks which form because of thermal contraction of a constrained plate which cannot contract in the along-ridge direction [*Turcotte*, 1974; *Sandwell*, 1986].

[32] Fracture zones must be weak for at least their first few million years to match the observed steps in gravity profiles. There is little sensitivity to differential subsidence after ~5 Myr (Figure 3). Therefore it is difficult to place reliable upper bounds on the duration of fracture zone weakness from gravity profiles, although the study of *Wessel and Haxby* [1990] is commonly misinterpreted as giving an upper bound of 4 Myr. This is more likely a lower bound. For fracture zones to remain weak for ~5 Myr consequently requires that fault zones in our model be deeper than ~10 km; otherwise, the thermal boundary layers conductively thicken to surround the fault zone, effectively locking it within this time (Figure 3c). On the basis of analysis of intraplate oceanic earthquakes with well-determined epicenters and focal mechanisms, there is statistically a slight tendency for such earthquakes to occur near fracture zones, indicating that these may be zones of weakness [*Bergman and Solomon*, 1992]. However, there is no evidence of preferential alignment of principal horizontal stresses perpendicular to fracture zones, as would be expected for a weak zone [*Bergman and Solomon*, 1992].

[33] The weakness of young fracture zones most likely reflects fault-weakening processes which accommodated strike-slip motion at transform faults. Two types of geophysical evidence suggest that transform faults are weak. First, the structural fabric of secondary faults near ridge transform intersections is most consistent with numerically modeled stress fields when the shear stress on transform faults is 3–5 times less than the normal stress at the ridge axis [*Phipps Morgan and Parmentier*, 1984] or the transform fault is almost completely (95%) mechanically decoupled [*Behn et al.*, 2002]. Second, both global [*Bird et al.*, 2002] and regional [*Okal and Langenhorst*, 2000] studies have shown

that recorded seismic moment release at transform faults is much less than that expected from plate motion models. These studies conclude that 80–90% of the plate motion across transforms is accommodated aseismically.

[34] Our models show that deflections to both gravity and bathymetry in the vicinity of fracture zones are enhanced by moderate amounts of extension or compression. For 2 km of extension or 1 km of convergence, gravity profiles across fracture zones are qualitatively similar to differential subsidence models. Slip which occurred earlier in a fracture zone's evolution could easily be overprinted by modest amounts of tectonic activity, and fracture zones could have their bathymetric and gravitational step rejuvenated and still qualitatively look similar to locked-fault, differential subsidence models. For >2 km of extension (or 1 km of convergence), however, bathymetry and gravity profiles should begin to manifest signatures diagnostic of tectonic overprinting, such as older-side ridges. A large number of profiles across Pacific fracture zones have older-side ridges (Figure 6) which we conclude are consistent with moderate extension. One explanation of linear, long-wavelength bands of alternating high and low gravity observed in eastern Pacific lithosphere [*Haxby and Weissel*, 1986] is that tensional far-field plate boundary forces have resulted in distributed lithospheric boudinage [*Sandwell et al.*, 1995]. (These have alternatively been hypothesized as small-scale convective rolls [*Haxby and Weissel*, 1986] aligned by plate shearing [*Richter*, 1973].) One problem with the tensional Pacific plate hypothesis is the lack of observed extensional faults parallel to the gravity ridges. However, if fracture zones are indeed weak heterogeneities, extension should primarily be accommodated at the fracture zones.

8. Conclusions

[35] Dynamic models of fracture zones that have weak faults (depth-averaged yield strength <10 MPa) have gravity offsets consistent with Pacific fracture zones. Previous studies have suggested that fracture zones must be weak for at least their first ~4 Myr, but gravity and bathymetry profiles of mature fracture zones in the east Pacific (Murray, Clarion, Clipperton, Galapagos, Marquesas, and Austral fracture zones) do not constrain how long fracture zones remain weak. Many profiles across these fracture zones have older-side highs which can be attributed to extension or alternatively to thermal stresses. Small-scale convection driven by local pressure gradients at a fracture zone results in modest thermal boundary layer removal and does not dramatically alter local bathymetry and gravity. Profiles across the Udintsev fracture zone, which extends back to its transform fault of origin, cannot be explained with models of simple cooling and subsidence with time and are most consistent with tectonic overprinting by moderate amounts of extension.

[36] **Acknowledgments.** We thank Y. Podladchikov and A. Poliakov for sharing their PARAVOZ program. We used GMT software developed by P. Wessel and W. Smith. This research has been supported by NSF grants EAR-0003558 and EAR-0337253. We thank D. Sandwell, P. Wessel, and an anonymous reviewer for constructive comments. Computations were performed at the Center for Advanced Computing Resources of the California Institute of Technology. This represents contribution 9088 of the Division of Geological and Planetary Sciences, California Institute of Technology.

References

Behn, M. D., J. Lian, and M. T. Zuber (2002), Evidence for weak oceanic transform faults, *Geophys. Res. Lett.*, *29*(24), 2207, doi:10.1029/2002GL015612.

Bercovici, D., H. J. B. Dick, and T. P. Wagner (1992), Nonlinear viscoelasticity and the formation of transverse ridges, *J. Geophys. Res.*, *97*, 14,195–14,206.

Bergman, E. A., and S. C. Solomon (1992), On the strength of oceanic fracture zones and their influence on the intraplate stress field, *J. Geophys. Res.*, *97*, 15,365–15,377.

Bird, P., Y. Y. Kagan, and D. D. Jackson (2002), Plate tectonics and earthquake potential of spreading ridges and oceanic transform faults, in *Plate Boundary Zones*, *Geodyn. Ser.*, vol. 30, edited by S. Stein and J. T. Freymueller, pp. 203–218, AGU, Washington, D. C.

Bonatti, E. (1978), Vertical tectonism in oceanic fracture zones, *Earth Planet. Sci. Lett.*, *37*, 369–379.

Bonneville, A., and M. K. McNutt (1992), Shear strength of the great Pacific fracture zones, *Geophys. Res. Lett.*, *19*, 2023–2026.

Byerlee, J. D. (1978), Friction of rocks, *Pure Appl. Geophys.*, *116*, 615–626.

Christeson, G. L., and M. K. McNutt (1992), Geophysical constraints on the shear stress along the Marquesas fracture zone, *J. Geophys. Res.*, *97*, 4425–4437.

Collot, J.-C., G. Lamarche, R. A. Wood, J. Delteil, M. Sosson, J.-F. Lebrun, and M. F. Coffin (1995), Morphostructure of an incipient subduction zone along a transform plate boundary: Puysegar ridge and trench, *Geology*, *23*, 519–522.

Cundall, P. A. (1989), Numerical experiments on localization in frictional materials, *Ing. Arch.*, *58*, 148–159.

Dick, H. J. B. (1989), Abysall peridotites, very slow spreading ridges and ocean ridge magmatism, in *Magmatism in the Ocean Basins*, edited by D. Saunders and M. J. Norry, *Geol. Soc. Spec. Publ.*, *42*, 71–105.

Escartin, J., G. Hirth, and B. Evans (1997), Nondilatant brittle deformation of serpentinites: Implications of Mohr-Coulomb theory and the strength of faults, *J. Geophys. Res.*, *102*, 2897–2913.

Gurnis, M., C. Hall, and L. Lavier (2004), Evolving force balance during incipient subduction, *Geochem. Geophys. Geosyst.*, *5*, Q07001, doi:10.1029/2003GC000681.

Hall, C. E., M. Gurnis, M. Sdrolias, L. L. Lavier, and R. D. Müller (2003), Catastrophic initiation of subduction following forced convergence across fracture zones, *Earth Planet. Sci. Lett.*, *212*, 15–30.

Haxby, W. F., and E. M. Parmentier (1988), Thermal contraction and the state of stress in the oceanic lithosphere, *J. Geophys. Res.*, *93*, 6419–6429.

Haxby, W. F., and J. K. Weissel (1986), Evidence for small-scale convection from Seasat altimeter data, *J. Geophys. Res.*, *91*, 3507–3520.

Karato, S.-I., and P. Wu (1993), Rheology of the upper mantle: A synthesis, *Science*, *260*, 771–778.

Kruse, S. E., M. C. McCarthy, M. R. Brudzinski, and M. E. Ranieri (1996), Evolution and strength of Pacific fracture zones, *J. Geophys. Res.*, *101*, 13,731–13,740.

Lavier, L. L., W. R. Buck, and A. N. B. Poliakov (2000), Factors controlling normal fault offset in an ideal brittle layer, *J. Geophys. Res.*, *105*, 23,431–23,442.

Lonsdale, P. (1994), Structural geomorphology of the Eltanin fault system and adjacent transform faults of the Pacific-Antarctic plate boundary, *Mar. Geophys. Res.*, *16*, 105–143.

Lowrie, A., C. Smoot, and R. Batiza (1986), Are oceanic fracture zones locked and strong or weak?: New evidence for volcanic activity and weakness, *Geology*, *14*, 242–245.

McCarthy, M. C., S. E. Kruse, M. R. Brudzinski, and M. E. Ranieri (1996), Changes in plate motions and the shape of Pacific fracture zones, *J. Geophys. Res.*, *101*, 13,715–13,730.

Meckel, T. A., M. F. Coffin, S. Mosher, P. Symonds, G. Bernandel, and P. Mann (2003), Underthrusting at the Hjort Trench, Australian-Pacific plate boundary: Incipient subduction?, *Geochem. Geophys. Geosyst.*, *4*(12), 1099, doi:10.1029/2002GC000498.

Menard, H. W., and T. Atwater (1968), Changes in direction of sea floor spreading, *Nature*, *219*, 463–467.

Menard, H. W., and T. Atwater (1969), Origin of fracture zone topography, *Nature*, *222*, 1037–1040.

Muller, M. R., C. J. Robinson, T. A. Minshull, R. S. White, and M. J. Bickle (1997), Thin crust beneath ocean drilling borehole 735B at the southwest Indian Ridge?, *Earth Planet. Sci. Lett.*, *148*, 93–107.

Müller, R. D., U. R. Roest, J.-Y. Royer, L. M. Gahagan, and J. G. Sclater (1997), Digital isochrons of the world's ocean floor, *J. Geophys. Res.*, *102*, 3211–3214.

Okal, E. A., and A. R. Langenhorst (2000), Seismic properties of the Eltanin transform system, South Pacific, *Phys. Earth Planet. Inter.*, *119*, 185–208.

Parmentier, E. M., and W. F. Haxby (1986), Thermal stresses in the oceanic lithosphere: Evidence from geoid anomalies at fracture zones, *J. Geophys. Res.*, *91*, 7193–7204.
Phipps Morgan, J., and D. W. Forsyth (1988), Three-dimensional flow and temperature perturbations due to a transform offset: Effects on oceanic crustal and upper mantle structure, *J. Geophys. Res.*, *93*, 2955–2966.
Phipps Morgan, J., and E. M. Parmentier (1984), Lithospheric stress near a ridge-transform intersection, *Geophys. Res. Lett.*, *11*, 113–116.
Poliakov, A. N. B., and H. J. Herrmann (1994), Self-organized criticality of plastic shear bands in rocks, *Geophys. Res. Lett.*, *21*, 2143–2146.
Poliakov, A. N. B., Y. Podladchikov, and C. Talbot (1993), Initiation of salt diapirs with frictional overburdens: Numerical experiments, *Tectonophysics*, *228*, 199–210.
Richter, F. M. (1973), Convection and the large-scale circulation of the mantle, *J. Geophys. Res.*, *78*, 8735–8745.
Saleeby, J. (1979), Kaweah serpentinite mélange, southwest Sierra Nevada foothills, California, *Geol. Soc. Am. Bull.*, *90*, 29–46.
Sandwell, D. T. (1984), Thermomechanical evolution of oceanic fracture zones, *J. Geophys. Res.*, *89*, 11,401–11,413.
Sandwell, D. T. (1986), Thermal stress and the spacings of transform faults, *J. Geophys. Res.*, *91*, 6405–6417.
Sandwell, D., and G. Schubert (1982), Lithospheric flexure at fracture zones, *J. Geophys. Res.*, *87*, 4657–4667.
Sandwell, D. T., and W. H. F. Smith (1997), Marine gravity anomaly from ERS-1, Geosat and satellite altimetry, *J. Geophys. Res.*, *102*, 10,039–10,045.
Sandwell, D. T., E. L. Winterer, J. Mammerickx, R. A. Duncan, M. A. Lynch, D. A. Levitt, and C. L. Johnson (1995), Evidence for diffuse extension of the Pacific plate from Pukapuka ridges and cross-grain gravity lineations, *J. Geophys. Res.*, *100*, 15,087–15,099.
Tucholke, B. E., and H. Schouten (1988), Kane fracture zone, *Mar. Geophys. Res.*, *10*, 1–39.
Turcotte, D. L. (1974), Are transform faults thermal contraction cracks?, *J. Geophys. Res.*, *79*, 2573–2577.
Uyeda, S., and Z. Ben-Avraham (1972), Origin and development of the Philippine Sea, *Nature Phys. Sci.*, *240*, 176–178.
Wessel, P., and W. F. Haxby (1990), Thermal stresses, differential subsidence, and flexure at oceanic fracture zones, *J. Geophys. Res.*, *95*, 375–391.

M. Gurnis and C. E. Hall, Seismological Laboratory, California Institute of Technology, Pasadena, CA 91125, USA. (chall@gps.caltech.edu)

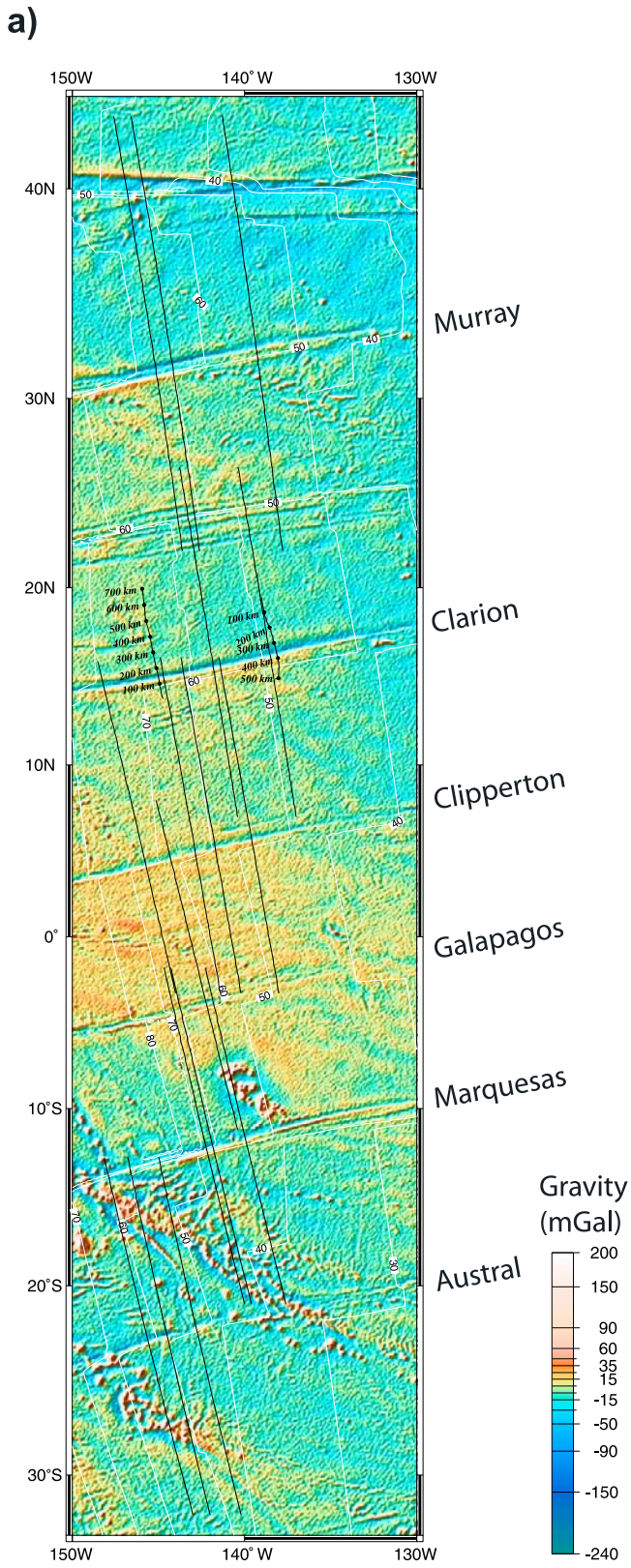

Figure 4. (a) Selected gravity profiles (black lines) across Pacific fracture zones. Black lines with circles at 100 km intervals are shipboard bathymetry profiles from survey HU931009. (b) Gravity profiles across the Udintsev and Menard fracture zones. The eastern and western branches of these fracture zones lie within the Antarctic and Pacific plates, respectively. Free-air gravity (shaded) is from *Sandwell and Smith* [1997] while seafloor age isochrons (white contours) are from *Müller et al.* [1997].

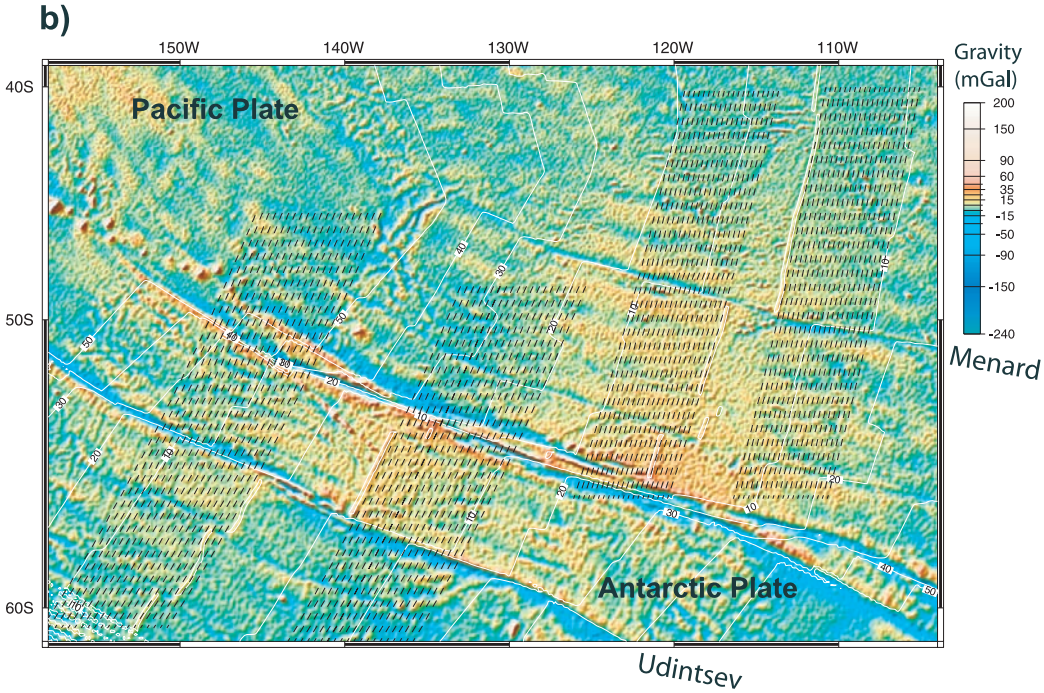

Figure 4. (continued)